Dalton Transactions

Accepted Manuscript

ROYAL SOCIETY OF CHEMISTRY

www.rsc.org/dalton

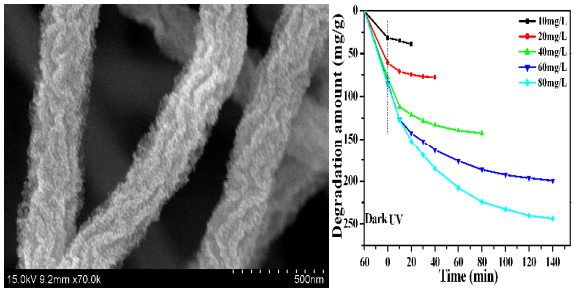

The porous ZnO/SnO_2 heteronanofibers were synthesized via electrospinning method, showing the enhanced photocatalysis for organic dyes degradation.

The synthesis of ZnO/SnO_2 porous nanofibers for dye adsorption and degradation

Xiang Chen, Feng Zhang, Qian Wang, Xiao Han, Xin Li, Jiuyu Liu, Huiming Lin *, Fengyu Qu*

College of Chemistry and Chemical Engineering, Harbin Normal University, P. R. China, Harbin 150025

Corresponding author: Tel/Fax: +86 0451 88060653.

E-mail address:qufengyu@ hrbnu.edu.cn and linhuiming@hrbnu.edu.cn

Abstract

ZnO/SnO_2 hetero-nanofibers about 250 nm in diameter and several micrometers in length are synthesized via electrospun method by using zinc chloride and stannous chloride as inorganic source. All fibers are composed of many nanoparticles (5-10 nm) that induce plenty of porous structure as well as high surface area. Under adjusting the ratio of zinc/stannous source, the synthesized porous ZnO/SnO_2 materials show various structures (corrugated fiber and tube), that is resulted from the different oxidation/decomposition temperature of the two components. Their photodegradation abilities toward various dye wastewaters (methylene blue, congo red, eosin red, and methyl orange) are demonstrated, showing the fast photodegradation and good recycle. It is noteworthy that ZnO/SnO_2 exhibits the enhanced photodegradation ability to congo red, ascribing to the high adsorption capacity derived from the strong electrostatic interaction between ZnO/SnO_2 and congo red. Based on the investigation, these porous ZnO/SnO_2 hetero-nanofibers possess versatile potential applications for wastewater purification.

Keywords: ZnO/SnO_2; porous nanofibers; electrospun; photocatalysis

1. Introduction

With the rapid progress of industry and development of society, the water pollution has been getting more serious than ever and becoming the first environmental problem in the world. Among the various water pollutions, the organic dyes have drawn extensive attention due to the high stability to temperature, light, and many chemicals. At present, physical adsorption and photocatalytic degradation are the two main means to treat the organic dye in wastewater. Photocatalytic degradation is considered as a "green" technique to offer great potential for complete degradation of organic dyes into pollution free [1].

Nanostructured semiconductor metal oxides, such as TiO_2, In_2O_3, Bi_2O_3, and Fe_2O_3 are widely used in photocatalysis, photoemission, and sensor etc.[2-8] ZnO, with the band gap of 3.37 eV and the large excitation binding energy (60 meV), is widely used in photocatalysis.[9-13] It is known that the large surface area always induces the high absorption capacity that benefits to photocatalysis. Currently, ZnO with various morphologies, such as: nanoflowers, nanosheets, nanospheres, and dendrites etc., have been prepared to enhance the surface area as well as the photocatalytic activity.[14-20] One-dimensional (1D) nanofibers, with high length-to-diameter ratio and ultra large special surface area, make the highly competitive advantage in photocatalysis.[21-24] Compared with the common methods such as chemical vapor deposition, hydrothermal and templateassisted, electrospun has been proved to be a versatile, effective, simple and inexpensive method to fabricate 1D nanofibers.[25-28] In addition, ZnO nanofibers synthesized from electrospun method always possess various porous structures to promote mass diffusion/transport and are configured as high performance in catalyst and sensor etc.

Furthermore, the fast recombination of the photo generated electron-hole pairs limits the photocatalytic efficiency. The effective separation of the photo-generated electrons and holes is considered as another route to improve the photocatalysis efficiency. Currently, the synthesis of heterostructure of semiconductor metal oxide is regarded as the effective method to enhance the photocatalytic activity by extending

the photoresponding range and increasing the electron hole pair separation efficiency.[29-35] Ag/ZnO heterostructure microspheres were prepared by Chai et al. via hydrothermal route, showing the enhanced photocatalytic performance (40 min) to Rhodamine B (10^{-5} mol/L) compared with pure ZnO. Wu et al. synthesized hierarchical ZnO/CdSe, which reveales the high photocatalytic character for the degradation of MB (20 mg/L) within 90 min.[36, 37]

Herein, ZnO/SnO_2 hetero-nanofibers were prepared by a simple electrospun method using zinc chloride and stannous chloride as inorganic sources and polyvinyl pyrrolidone (PVP) as the thickener agent. Under adjusting the amount of zinc/ stannous source, the ZnO/SnO_2 nanofibers with different structure were obtained. And the formation mechanism was also deduced. The photocatalytic degradation of these synthesized ZnO/SnO_2 nanofibers toward methylene blue, Congo red, eosin red, and methyl orange has been investigated in detail.

2. Experimental

2.1 Materials

Polyvinylpyrrolidone (PVP, Mw=1,300,000), zinc chloride and stannous chloride were purchased from Aladdin (China). N, N-dimethylformamide (DMF) was bought from Tianjin Fengchuan Chemical Co. (China). Congo red (CR), methylene blue (MB), methyl orange (MO), eosin red (ER) were bought from Tianjin Guangfu Chemical Co. (China). All the reagents were of analytical grade and used without further purification.

2.2 Synthesis of the ZnO/SnO_2 hetero-nanofibers

In a typical procedure, zinc chloride and stannous chloride amount to 0.72 g (the mass ratio of zinc chloride and stannous chloride was 1:3, 1:1, 3:1 respectively) were dissolved in 4.2 g of DMF under stirring for 2 h, and then 0.6 g of PVP was added into the resulting solution with continuous stir for 4h at room temperature to form the uniform precursor. The obtained viscous precursor solution was then loaded into a 5 ml syringe connected to 9-gauge stainless steel needle. A variable high voltage power supply (Gamma FL 32174) was used to provide a high voltage (15 kV) for the electrospinning of as-prepared solutions. The positive electrode of the high voltage

power supply was connected to the needle tip and the grounded electrode was connected to a metallic collector wrapped with an aluminum foil. Dry fibers were accumulated on the aluminum foil and collected as a fibrous mat. The final ZnO/SnO_2 hetero-nanofibers were eventually obtained after calcined at 600℃ for 3 h in air. The samples synthesized using different mass ratio of zinc chloride and stannous chloride were designated as ZnO/SnO_2-1, ZnO/SnO_2-2, and ZnO/SnO_2-3.

2.3 Photocatalytic tests

The photocatalytic activity was evaluated by the degradation of methylene blue (MB), Congo red (CR), eosin red (ER), and methyl orange (MO), respectively. In a typical process, 0.05 g as-fabricated material was suspended in 200 ml methylene blue aqueous solution (10 mg l^{-1}). The suspensions were magnetically stirred in the dark to ensure an adsorption/desorption equilibrium, and the solution was then exposed to an 500 W mercury lamp at room temperature. At given irradiation time intervals, the samples were collected regularly to measure the methylene blue degradation by UV-vis spectroscopy. Finally, the experiments of the photocatalytic degradation of Congo red, eosin red and methyl orange aqueous solution were also conducted under the same conditions

2.4 Characterization of the samples

The crystalline phase of the synthesized samples was determined by X-ray powder diffraction (XRD, Rigaku Dmax-rB, Cu K*a* radiation, λ= 0.1542 nm 40 KV, 100 mA). The nitrogen adsorption/desorption was measured using a Micromeritics ASAP 2010M sorptometer. Specific surface areas and pore size distributions were calculated using the Brunauer-Emmett-Teller (BET) and Density Functional Theory (DFT) models from the adsorption branches, respectively. Before measured at 77 K, the samples were degassed at 393 K for 12 h. The morphology and structure of the product were studied by scanning electron microscopy (SEM, Hitachi-4800) and transmission electron microscopy (TEM, JEOL 2010, 200kV). Zeta potential and dynamic light scattering (DLS) was carried out with ZetaPALS Zeta Potential Annlyze. Thermal gravimetry-differential thermal analysis (TG-DTA) was studied with Diamond 6300.

3. Results and discussion

The morphology and structure of as-synthesized ZnO/SnO_2 nanofibers were investigated by TEM and SEM. Fig.1a and b show the low and high magnification SEM image of ZnO/SnO_2-2. From 1a, ZnO/SnO_2-2 reveals the uniform nanofibers with about 250 nm in diameter and several micrometers in length. As shown in the high magnification SEM image, every fiber exhibits rough and corrugated surface. The microstructure of the ZnO/SnO_2-2 nanofibers was further investigated by TEM observations. As displayed in Fig.1c, the nanofibers of ZnO/SnO_2-2 are composed of many nanoparticles about 5-10 nm in size. And the gaps of these accumulational nanaoparticles bring abundant porous structure of ZnO/SnO_2-2. The high-resolution TEM image of ZnO/SnO_2-2 is shown in Fig. 1d, the interplanar distance of 0.34 nm is close to the d-spacing of (110) plane of the tetragonal rutile SnO_2. The interplanar distance of 0.28 nm agrees well with the lattice spacing of the (100) planes of the hexagonal wurtzite ZnO. Furthermore, Fig. 1e and Fig. 1f show the STEM image and the EDS line scan analysis results corresponds to the red line in Fig. 1e. From Fig. 1f, Zn, Sn and O element are present along the compositional line and share a similar intensity trend, indicating the homogeneous dispersion of Zn, Sn, and O in the fiber that is help for the electron transition between ZnO and SnO2. Moreover, there are little spatial distributions for the atomic composition, which is in accordance well with the corrugated structure as shown in STEM and TEM images (Fig. 1c and e).

Besides ZnO/SnO_2-2, ZnO/SnO_2-1 and ZnO/SnO_2-3, with different mass ratio of zinc chloride and stannous chloride (1:3 and 3:1), were prepared as the comparison. Fig. 2 shows the SEM and TEM images of ZnO/SnO_2-1 and ZnO/SnO_2-3. From Fig. 2a, ZnO/SnO_2-1 reveals the tube structure with 250 nm in diameter. As displayed in Fig. 2d, ZnO/SnO_2-3 also exhibits the tube structure (500 nm) built by the accumulation of many nanorods (30 nm in width and 100 nm in length, Fig. 2e). And the high resolution TEM images (Fig. 2c and f) further confirm that their hollow structures are accumulated by the ZnO and SnO_2 nanoparticles. As displayed in Fig. 1 and 2, the particle size of ZnO/SnO_2-2 is about 5-10 nm, while that of ZnO/SnO_2-1

and ZnO/SnO_2-3 increases to 15-20 and 25-30 nm, respectively. That is because with the similar amount of Zn and Sn (1:1) ZnO/SnO_2-2 primary fibers possess great mixing extent of Zn and Sn source that induce the uniform nucleation/growth process of ZnO and SnO_2 and the small particle size as well. A possible formation mechanism of the hollow structure may be proposed as follows: when the precursor solution (zinc chloride, stannous chloride, PVP, and DMF) was spun from the syringe, the primary fibers were obtained on the aluminum foil with the volatilization of DMF. And then they were calcined in air to undergo the oxidation/decomposition of zinc chloride and stannous chloride to form ZnO and SnO_2. At the same time, calcination treatment also makes PVP decomposed and oxidized. And decomposition of these precursors would produce plenty of gases, such as CO_2 and steam, which induces the pressure difference between the inner and the outside to result the hollow structure.[38] Furthermore, TG-DTA was also used to reveal the formation process. From Fig. 3 the oxidation/decomposition of PVP-stannous chloride occurs at 300-500 ℃ while that of PVP-zinc chloride takes place at 400-600 ℃. As the synthesis of ZnO/SnO_2-1 (Sn:Zn=3:1) and ZnO/SnO_2-3 (Sn:Zn=1:3), the oxidation/decomposition depends on the major component that generates enough pressure difference between the inner and the outside of the nanofibers to make the nanoparticles tend to outside [38]. So, ZnO/SnO_2-1 and ZnO/SnO_2-3 display the hollow tube structure. However, with the similar amount of Zn and Sn source, ZnO/SnO_2-2 possess two oxidation/decomposition processes (300 to 600 ℃) derived from the two component so that there is not enough pressure difference for the hollow structure but the corrugated surface at last.

The X-ray diffraction (XRD) patterns of the as-electrospun ZnO/SnO_2-1, ZnO/SnO_2-2 and ZnO/SnO_2-3 hetero-nanofibers are shown in Fig. 4, which provides further insight into the crystallinity of the products. All the diffraction peaks could be well indexed as the hexagonal wurtzite structure for ZnO (JCPDS 36-1451) and the tetragonal rutile structure for SnO_2 (JCPDS 41-1445), respectively. From Fig. 4, the increase of the diffraction intensity of ZnO from ZnO/SnO_2-1 to ZnO/SnO_2-3,

implying the enhanced crystallinity derived from the increase of the amount of ZnO. Furthermore, no other peaks indicate the purity of these samples. In addition, from Fig. 4, ZnO/SnO_2-2 reveals the wider diffraction peaks than that of ZnO/SnO_2-1 and ZnO/SnO_2-3, suggesting the smaller particle size of ZnO/SnO_2-2. That is also consistent with the result from TEM images.

The porous structures of the as-fabricated ZnO/SnO_2 nanofibers were further analyzed by nitrogen sorption isotherm techniques. Fig. 5 presents the nitrogen adsorption-desorption isotherms and BJH pore size distribution curves of all samples. As observed in Fig. 5a, all ZnO/SnO_2 nanofibers exhibit the type IV isotherms with H_3 hysteresis loops at high relative pressure region (P/P_0 = 0.7-1), implying the split porous structure originated from the accumulation of nanoparticles. That agrees with the result of TEM. From Fig. 1 and 2, the nanofibers are composed by many nanparticles about 5-30 nm in size and their split porous structure also can be found from the high magnified TEM images. The corresponding pore size distribution curves were obtained by the BJH method as displayed in Fig. 5b. The pore size of ZnO/SnO_2-1 centers at about 3.3 and 7.4 nm, and ZnO/SnO_2-2 reveals the pore distribution at 3.3, 5.4, and 8.2 nm. However, ZnO/SnO_2-3 exhibits low porosity with pore size at about 3.3 and 5.4 nm. In addition, the BET analysis reveals the surface area of ZnO/SnO_2-1, ZnO/SnO_2-2, and ZnO/SnO_2-3 is 30.175, 39.344, and 11.063 m^2/g, respectively (Table 1). The largest surface area of ZnO/SnO_2-2 is ascribed to the corrugated porous structure and the small particle size.

These ZnO/SnO_2 nanofibers were adopted as the catalysts and the photocatalytic degradation testing toward methylene blue (MB) was carried out. Fig. 6a-c presents the absorption spectra of MB aqueous solution (initial concentration is 10 mg/L) in the presence of the ZnO/SnO_2 nanofibers under exposure to UV light for different durations. With the increase of the irradiation time, the absorption peak corresponding to MB at 663 nm diminishes gradually, testifying the degradation of MB. As shown in Fig. 6, under UV light irradiation for 35 min, 97.3 % of MB is decomposed by using the ZnO/SnO_2-2 as the photocatalyst, while at the same time ZnO/SnO_2-1 and

ZnO/SnO_2-3 reveal 94.3 and 84.5 % degradation. And it takes 45 and 65 min for ZnO/SnO_2-1 and ZnO/SnO_2-3 to reach 96.6 and 97.7 % of decolorization, respectively. In addition, the commercial ZnO and SnO_2 were used as the contrast and the photocatalytic degradation performance was also investigated. From Fig. 6d and e, 100 min is needed to decompose 98.6 % and 97.7 % MB for ZnO and SnO_2 nanofibers, respectively.

In order to further investigate the photocatalytic activites of these samples, the photocatalytic degradation kinetics was analyzed using pseudo-first-order kinetics:

$$\ln (C_0 / C) = kt$$

Where k is a pseudorst-rate kinetic constant (min^{-1}), t is the irradiation time (min), C is the concentration and C_0 means the initial concentration (mg/L) of the reactant. The variations in $\ln(C/C_0)$ as a function of irradiation time are given in Fig. 6f. From Fig. 6f, all samples exhibit the good linear relationship between $\ln(C/C_0)$ and irradiation time t. The reaction rate constant (slope of the fitting line) of ZnO/SnO_2-1, ZnO/SnO_2-2, ZnO/SnO_2-3, ZnO, and SnO_2 is 0.07417, 0.102337, 0.05742, 0.05118, and 0.04599 min^{-1}, respectively. As shown in Fig. 6f, ZnO/SnO_2 nanofibers possess the faster reaction rate than ZnO and SnO_2 that is ascribed to the heterostructure of ZnO/SnO_2. Furthermore, it can be seen that the decomposition rate of ZnO/SnO_2 nanofibers is as follows: ZnO/SnO_2-2> ZnO/SnO_2-1>ZnO/SnO_2-3. The enhanced degradation rate of ZnO/SnO_2-2 lies on its large surface area (39.344 m^2/g), the small particle size (5-10 nm) and the mass ratio of Zn/Sn source.

Considering the good performance of ZnO/SnO_2-2 on dye treatment, photocatalytic degradation activities of ZnO/SnO_2-2 nanofibers to Congo red (CR), methyl orange (MO), eosin red (ER) dyes were also investigated. Fig. 7 displays the UV/Vis adsorption spectra of dyes in the presence of ZnO/SnO_2-2 nanofibers under UV light at different time intervals. When the light was turned on, the main peaks decreased continuously with the increase of irradiation time, indicating that the dyes were decomposed. As exhibited in Fig. 7a the intensity of the absorbance peaks at 500 nm drops rapidly with the elongation of the exposure time and completely disappears after about 20 min (efficiency up to 98.8 %). From Fig. 7b, when the illumination

time is extended to 100 min, the color of MO solution vanishes with the photocatalytic degradation efficiency up to 97.7 % (at 461 nm). And Fig. 7c illustrates the photodegradation of 98.9% ER (at 515 nm) after 70 min irradiation. And the degradation rate curves are summarized in Fig. 7d, after the dark adsorption for 60 min, ZnO/SnO_2-2 reveals 78.29 % adsorption toward CR, while the adsorption decreases to 0 %, 1.15 % and 9.34 % for MO, MB and ER, respectively. It is believed that, the high photodegradation efficiency of ZnO/SnO_2-2 to CR can be ascribed to the high adsorption amount of CR.

Considering the good photo-degradation of ZnO/SnO_2-2 toward CR, various CR solutions (20-80 mg/L) was used to further demonstrate the adsorption and degradation activity of ZnO/SnO_2-2. From Fig. 8a-d, as the illumination time goes on, the adsorption peaks decreases continuously, indicating that the dyes were decomposed. As shown in Fig. 8a-d, it costs 40, 80, 140 and 140 min for ZnO/SnO_2-2 to decompose about 96.8 % (20 mg/L), 89.3 % (40 mg/L), 83.1% (60mg/L), and 76.0 % (80 mg/L) CR, respectively. And the equilibrium adsorption isotherm (dark adsorption) of ZnO/SnO_2-2 to CR solution was calculated as exhibited in Fig. 8e. With the increase of the dye concentration, the adsorption amount increases dramatically until the adsorption reaches saturation (85.8 mg/g) that is a rather high adsorption amount compared with the previous reports.[39] Furthermore, as shown in Fig. 8e, the adsorption isotherm belongs to a type I curve, characteristic of a Langmuir isotherm. And the experimental equilibrium adsorption of dye on the sample was also analyzed by fitting the equilibrium adsorption data using the Langmuir equation:

$$\frac{c_e}{q_e} = \frac{1}{q_m k} + \frac{c_e}{q_m}$$

Where q_m is the theoretical maximum monolayer adsorption capacity (mg/g), k is the Langmuir constant, c_e is equilibrium concentration, and q_e is the equilibrium adsorption amount (mg/g). The corresponding linear Langmuir transform of the

isotherm is exhibited in the Fig. 8e inset. From Fig. 8e inset, the adsorption behavior displays a good linear Langmuir relationship with the theoretical maximum adsorption values (q_m = 90.8 mg/g) close to the experimental capacities (85.8 mg/g). It is known that, CR is a typical anionic dye, and the strong electrostatic interaction between CR and positive ZnO/SnO_2-2 (zeta potential: 9.71 ± 4.22 mV) nanofibers induces the high adsorption amount. The good Langmuir adsorption relationship between CR and ZnO/SnO_2-2 associated with the high adsorption amount are expected to bring up the enhanced degradation capability [39].

In addition, the variation of the degradation capability (dye/catalyst, mg/g) to degradation time was recorded as displayed in Fig. 8f. ZnO/SnO_2-2 displays 39.07 mg/g degradation capability for 10 mg/L CR under irradiation for 20 min. With the increase of CR concentration, the degradation capability increases to 152.06 mg/g (20 min) for 80 mg/L CR and after 140 min the degradation capability can reach 234.5 mg/g. Moreover, the TG-DTA analysis of ZnO/SnO_2-2, after the treatment of 80 mg/L CR solution for 140 min, was carried out. From Fig. 9, the residue dye in ZnO/SnO_2-2 after the photocatalysis is just 4.0 % (the weight loss between 200-500 ℃). That further confirms that the high effective purification ability of ZnO/SnO_2-2 toward CR depends on photodegradation rather than the physical adsorption. The high adsorption capacity benefits the dye molecules to be adsorbed on to the surface of the catalyst to induce the high photocalalysis performance.

The improved photocatalytic activity found for the ZnO/SnO_2 heterostructure nanofibers can be explained as follow: When the ZnO/SnO_2 heterojunction was excited by UV light with a photon energy higher or equal to the band gaps of ZnO and SnO_2, the electrons in the VB could be excited to the CB with simultaneous generation of the same amount of holes in the VB. From the energy band structure diagram of the ZnO/SnO_2 heterojunction, it could be found that the photogenerated electron transfer occurred from the CB of ZnO to the CB of SnO_2 and, conversely, the photogenerated hole transfer could take place from the VB of SnO_2 to the VB of ZnO, suggesting that the photogenerated electrons and holes were efficiently separated. The

photocatalytic mechanism in our experiment was proposed as follows:

$$(ZnO/SnO_2) + hV \longrightarrow (SnO_2)\, e^- + (ZnO)\, {}^{+}h$$

$$(SnO_2)\, e^- + O_2 \longrightarrow O_2^{\bullet -}$$

$$(ZnO)\, h^+ + OH^- \longrightarrow OH^{\bullet}$$

$$O_2^{\bullet -} + H_2O \longrightarrow HO_2^{\bullet} + OH^-$$

$$HO_2^{\bullet} + H_2O \longrightarrow H_2O_2 + OH^{\bullet}$$

$$H_2O_2 \longrightarrow 2OH^{\bullet}$$

$$CR + 2OH^{\bullet} \longrightarrow \text{degradation product}$$

The resulting charge carrier separation leads to increased carrier lifetime because of reduced charge recombination. As a consequence, the formation of hydroxyl $OH^{\bullet}$ radicals by reaction of holes with surface hydroxyl groups or physisorbed water molecules at the zinc oxide surface is enhanced. On the other side, also the reaction of electrons with dissolved oxygen molecules to give superoxide radical anions, $O_2^{\bullet -}$, yielding hydroperoxyl radicals $HO_2^{\bullet}$ on protonation and finally $OH^{\bullet}$ radicals will be more efficient. $OH^{\bullet}$ Radicals are a strong oxidizing agent well-known to decompose organic substrates as CR dye. As a result, the enhanced charge separation related to the ZnO/SnO_2 heterojunction favors the interfacial charge transfer to physisorbed species forming $OH^{\bullet}$ radicals and reduce possible back reactions, and therefore result in the higher activity of the ZnO/SnO_2 heterostructure nanofibers.

In addition, the recycle ability of ZnO/SnO_2-2 was also studied. From Fig. 10, after the 5 recycle, the photocatalytic efficiency also can remain 95.5% (20 min, CR). The well recycle ability is significant for catalysts to be used in practical application.

4. Conclusions

In summary, ZnO/SnO_2 nanofibers were synthesized by a simple electrospun method. By adjusting the mass ratio of Zn/Sn sources, porous nanofibers and nanotubes was obtained due to the oxidation/decomposition of the precursors. All the fibers/tubes are accumulated by many nanoparticles (5-30 nm) that make the porous

structure and large surface of the samples. MB, CR, eosin red, and MO were adopted as the typical dyes and the photocatalysis behavior was carried out in detail. ZnO/SnO_2 nanofibers shows the enhanced photocatalytic ability due to the effective separation of the photo-generated electrons/holes and high adsorption capacity. Moreover, ZnO/SnO_2-2 possess the high adsorption capacity (up to q_m= 90.8 mg/L) to CR, a typical anionic dye, profited from the strong electrostatic interaction between CR and ZnO/SnO_2-2 (positive charge). In the favor of the high adsorption capacity, ZnO/SnO_2-2 also induces the highest photocatalytic ability toward CR than other dyes (MO, MB and ER). These porous ZnO/SnO_2 hetero-nanofibers show potential application in wastewater treatment. Based on the above investigation, the porous structure, hetero-structure, strong interaction between catalysts and dye should be considered in the synthesis of the catalysts with the enhanced photodegradation ability.

Acknowledgements

Financial support for this study was provided by the National Natural Science Foundation of China (21471041, 21171045, 21101046, 21441002, 21403048), Natural Science Foundation of Heilongjiang Province of China ZD201214.

References

1. Michael R. Hoffmann, Scot T. Martin, Wonyong Choi and D. W. Bahnemann, *Chem. Rev*., 1995, 95, 69-96.

2. V. Kuzhalosai, B. Subash, A. Senthilraja, P. Dhatshanamurthi and M. Shanthi, *Spectrochimica acta. Part A, Molecular and biomolecular spectroscopy*, 2013, 115, 876-882.

3. Y. Min, K. Zhang, Y. Chen and Y. Zhang, *Chemical Engineering Journal*, 2011, 175, 76-83.

4. R. Nakano, R. Chand, E. Obuchi, K. Katoh and K. Nakano, *Chemical Engineering Journal*, 2011, 176–177, 260-264.

5. Y. Shi, H. Li, L. Wang, W. Shen and H. Chen, *ACS applied materials & interfaces*, 2012, 4, 4800-4806.

6. J. S. Jang, K. Y. Yoon, X. Xiao, F.-R. F. Fan and A. J. Bard, *Chemistry of Materials*, 2009, 21, 4803-4810.

7. T. Xie, C. Liu, L. Xu, J. Yang and W. Zhou, *The Journal of Physical Chemistry C*, 2013, 117, 24601-24610.

8. H. Fan, H. Li, B. Liu, Y. Lu, T. Xie and D. Wang, *ACS applied materials & interfaces*, 2012, 4, 4853-4857.

9. C. Shifu, Z. Wei, Z. Sujuan and L. Wei, *Chemical Engineering Journal*, 2009, 148, 263-269.

10. C. Shifu, Z. Wei, L. Wei, Z. Huaye and Y. Xiaoling, *Chemical Engineering Journal*, 2009, 155, 466-473.

11. M. Faisal, A. A. Ismail, A. A. Ibrahim, H. Bouzid and S. A. Al-Sayari, *Chemical Engineering Journal*, 2013, 229, 225-233.

12. W. S. Chiu, P. S. Khiew, M. Cloke, D. Isa, T. K. Tan, S. Radiman, R. Abd-Shukor, M. A. A. Hamid, N. M. Huang, H. N. Lim and C. H. Chia, *Chemical Engineering Journal*, 2010, 158, 345-352.

13. S. Meshram, R. Limaye, S. Ghodke, S. Nigam, S. Sonawane and R. Chikate, *Chemical Engineering Journal*, 2011, 172, 1008-1015.

14. T. Tao, A. M. Glushenkov, H. Liu, Z. Liu, X. J. Dai, H. Chen, S. P. Ringer and Y. Chen, The *Journal of Physical Chemistry C*, 2011, 115, 17297-17302.

15. H. Wang, T. You, W. Shi, J. Li and L. Guo, *The Journal of Physical Chemistry C*, 2012, 116, 6490-6494.

16. P. Manjula, R. Boppella and S. V. Manorama, *ACS applied materials & interfaces*, 2012, 4, 6252-6260.

17. Y. Yan, Q.-S. Wu, Li and Y.-P. Ding, *Crystal Growth & Design*, 2006, 6, 769-773.

18. W.-T. Yao, S.-H. Yu, S.-J. Liu, J.-P. Chen, X.-M. Liu and F.-Q. Li, *The Journal of Physical Chemistry B*, 2006, 110, 11704-11710.

19. X. Song, Y. Zhao, H. Wang and Q. Du, *Langmuir*, 2009, 25, 4443-4449.

20. Z. Yu, F. Qu and X. Wu, *Dalton transactions*, 2014, 43, 4847-4853.

21. C.-H. Lin, J.-H. Chao, C.-H. Liu, J.-C. Chang and F.-C. Wang, *Langmuir*, 2008, 24, 9907-9915.

22. J. Mu, B. Chen, M. Zhang, Z. Guo, P. Zhang, Z. Zhang, Y. Sun, C. Shao and Y. Liu, *ACS applied materials & interfaces*, 2011, 4, 424-430.

23. D. Yang, H. Liu, Z. Zheng, Y. Yuan, J.-c. Zhao, E. R. Waclawik, X. Ke and H. Zhu, *Journal of the American Chemical Society*, 2009, 131, 17885-17893.

24. J. Mu, C. Shao, Z. Guo, Z. Zhang, M. Zhang, P. Zhang, B. Chen and Y. Liu, *ACS applied materials & interfaces*, 2011, 3, 590-596.

25. S. K. Lim, S.-H. Hwang, D. Chang and S. Kim, *Sensors and Actuators B: Chemical*, 2010, 149,

28-33.
26. J. Di, H. Chen, X. Wang, Y. Zhao, L. Jiang, J. Yu and R. Xu, *Chemistry of Materials*, 2008, 20, 3543-3545.
27. A. Abdal-hay, J. Lim, M. Shamshi Hassan and J. K. Lim, *Chemical Engineering Journal*, 2013, 228, 708-716.
28. H. R. Pant, P. Risal, C. H. Park, L. D. Tijing, Y. J. Jeong and C. S. Kim, *Chemical Engineering Journal*, 2013, 221, 90-98.
29. L. Zheng, Y. Zheng, C. Chen, Y. Zhan, X. Lin, Q. Zheng, K. Wei and J. Zhu, *Inorganic chemistry*, 2009, 48, 1819-1825.
30. C. Cheng, B. Liu, H. Yang, W. Zhou, L. Sun, R. Chen, S. F. Yu, J. Zhang, H. Gong, H. Sun and H. J. Fan, *ACS Nano*, 2009, 3, 3069-3076.
31. W. W. Wang, Y. J. Zhu and L. X. Yang, *Advanced Functional Materials*, 2007, 17, 59-64.
32. W. Zhou, H. Liu, J. Wang, D. Liu, G. Du and J. Cui, *ACS applied materials & interfaces*, 2010, 2, 2385-2392.
33. F.-X. Xiao, *ACS applied materials & interfaces*, 2012, 4, 7055-7063.
34. J.-W. Xu, Z.-D. Gao, K. Han, Y. Liu and Y.-Y. Song, *ACS applied materials & interfaces*, 2014, 6, 15122-15131.
35. G. Luo, X. Jiang, M. Li, Q. Shen, L. Zhang and H. Yu, *ACS applied materials & interfaces*, 2013, 5, 2161-2168.
36. B. Chai, X. Wang, S. Cheng, H. Zhou and F. Zhang, *Ceramics International*, 2014, 40, 429-435.
37. Y. Wu, F. Xu, D. Guo, Z. Gao, D. Wu and K. Jiang, *Applied Surface Science*, 2013, 274, 39-44.
38. L. Lang, D. Wu and Z. Xu, *Chemistry*, 2012, 18, 10661-10668.
39. S. Lan, L. Liu, R. Li, Z. Leng and S. Gan, *Industrial & Engineering Chemistry Research*, 2014, 53, 3131-3139.

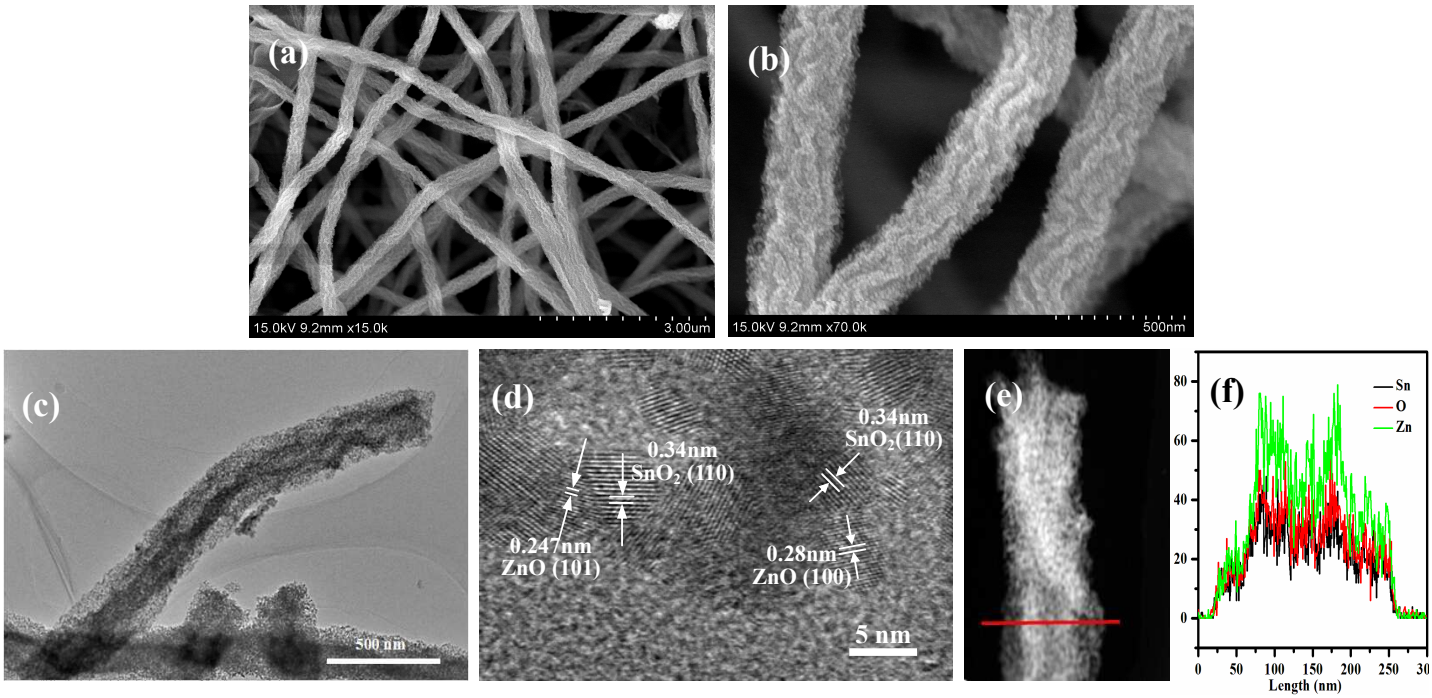

Fig. 1 (a-b) SEM and (c-d) TEM images of ZnO/SnO_2-2; (e) STEM image of a single fiber; (f) Compositional line profiles across the fiber along the line as marked by the red line in (e).

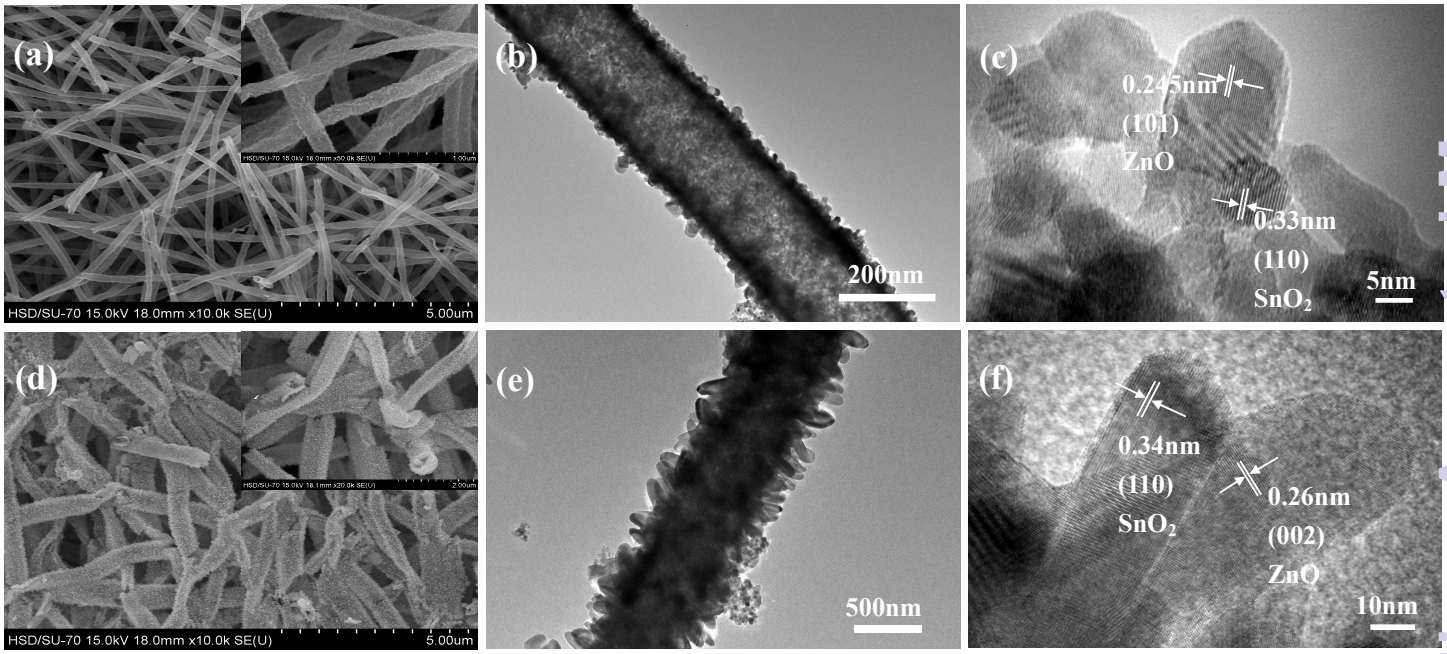

Fig. 2 SEM images of ZnO/SnO_2-1 (a) and ZnO/SnO_2-3 (d) with the corresponding high magnification image inset. TEM images of ZnO/SnO_2-1 (b, c) and ZnO/SnO_2-3 (e, f).

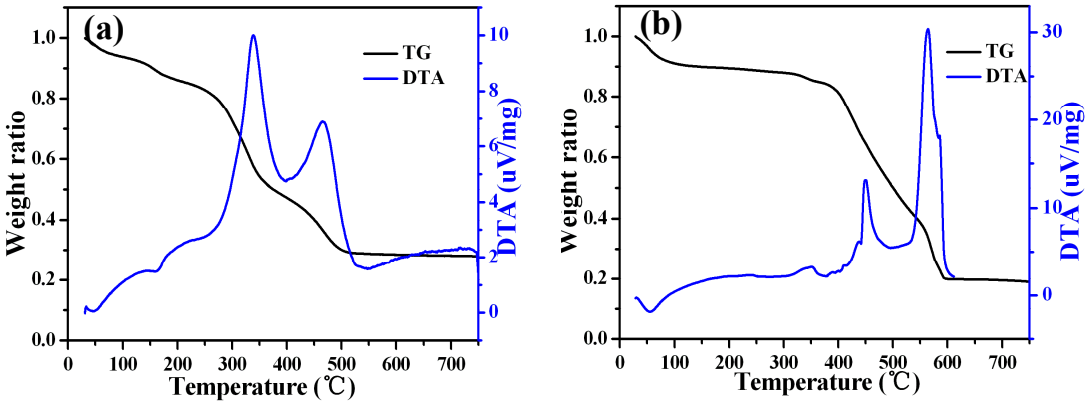

Fig. 3 Thermal gravimetry-differential thermal analysis (TG-DTA) curves of PVP-stannous chloride (a) and PVP- zinc chloride (b) composite fibers.

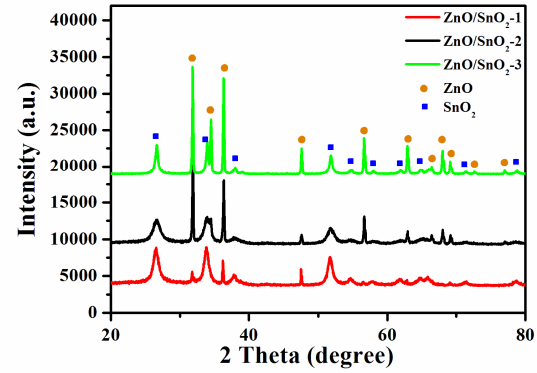

Fig. 4 XRD patterns of the as-synthesised ZnO/Sn_2O-1, ZnO/Sn_2O-2 and ZnO/Sn_2O-3 nanofibers.

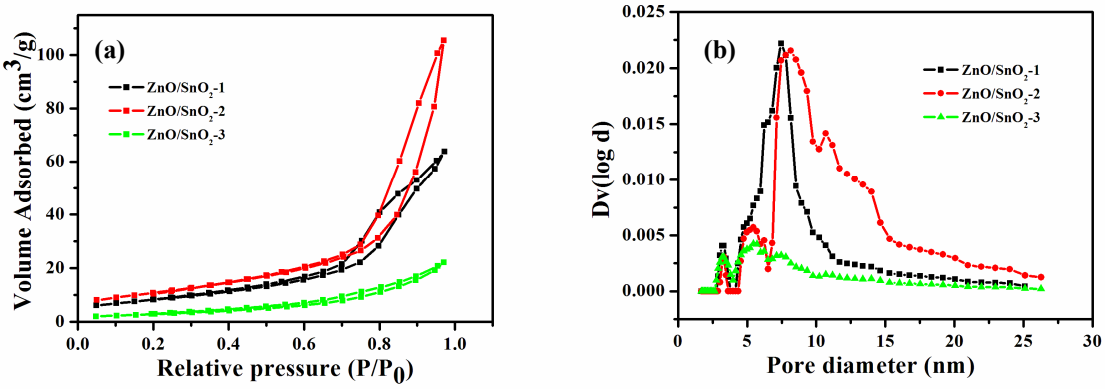

Fig. 5 N_2 adsorption-desorption isotherm (a) and BJH pore size distribution (b) of the samples.

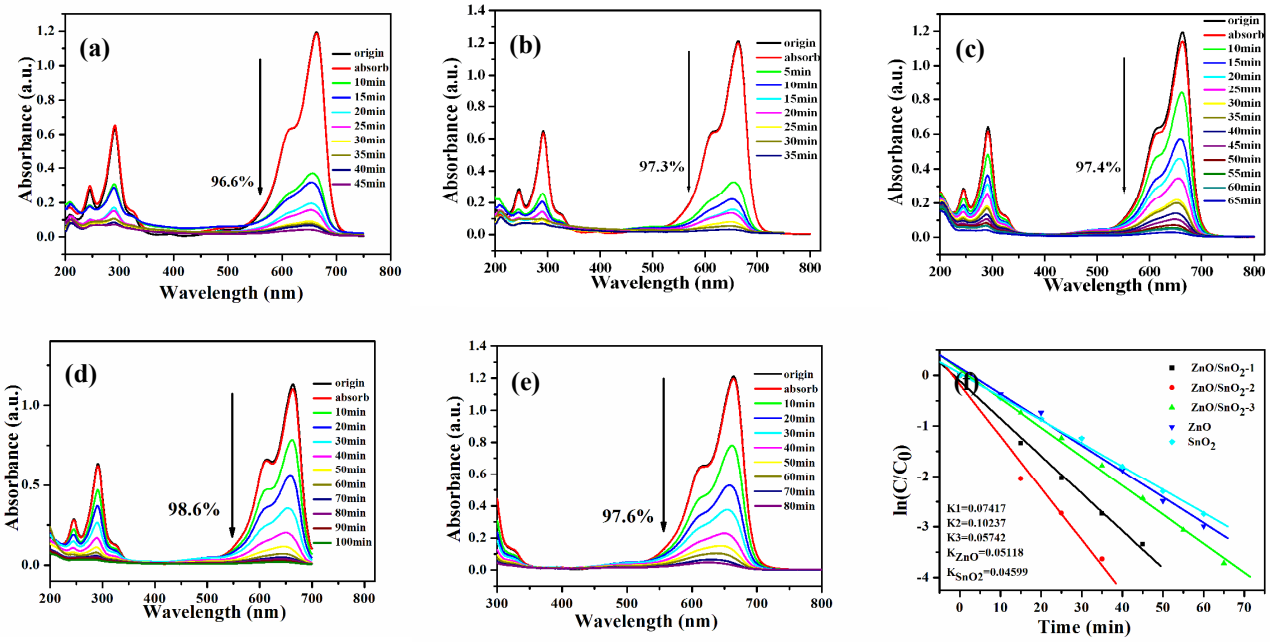

Fig. 6 Adsorption spectra of methylene blue solution under UV light in the presence of (a) ZnO/SnO_2-1, (b) ZnO/SnO_2-2, (c) ZnO/SnO_2-3, (d) ZnO nanofibers, (e) SnO2 nanofibers, (f) Kinetic linear simulation curves of MB with different electrospun nanofibers.

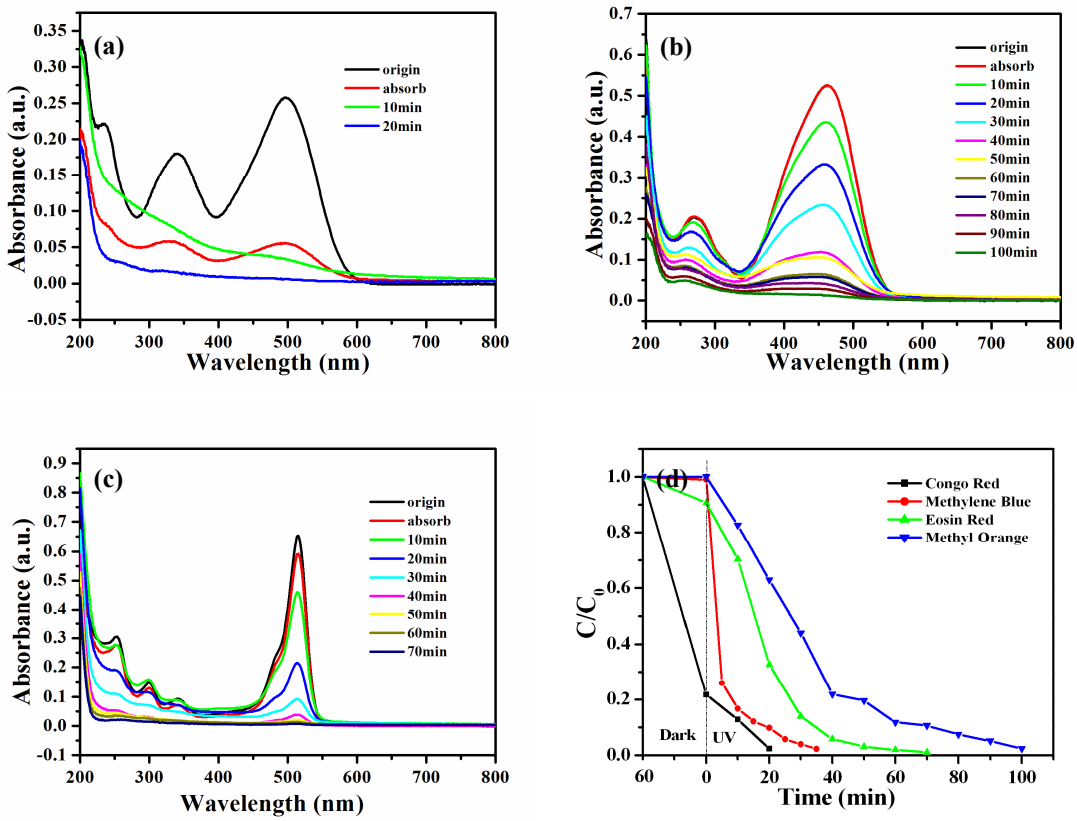

Fig. 7 Variations of adsorption spectra of organic dye solutions in the presence of the ZnO/SnO_2-2 heterostructure nanofiber irradiated by a mercury lamp for varying times; (a) Congo red, (b) methyl orange, (c) eosin red, (d) the ZnO/SnO_2-2 photocatalysis degradation rate of the four organic dyes.

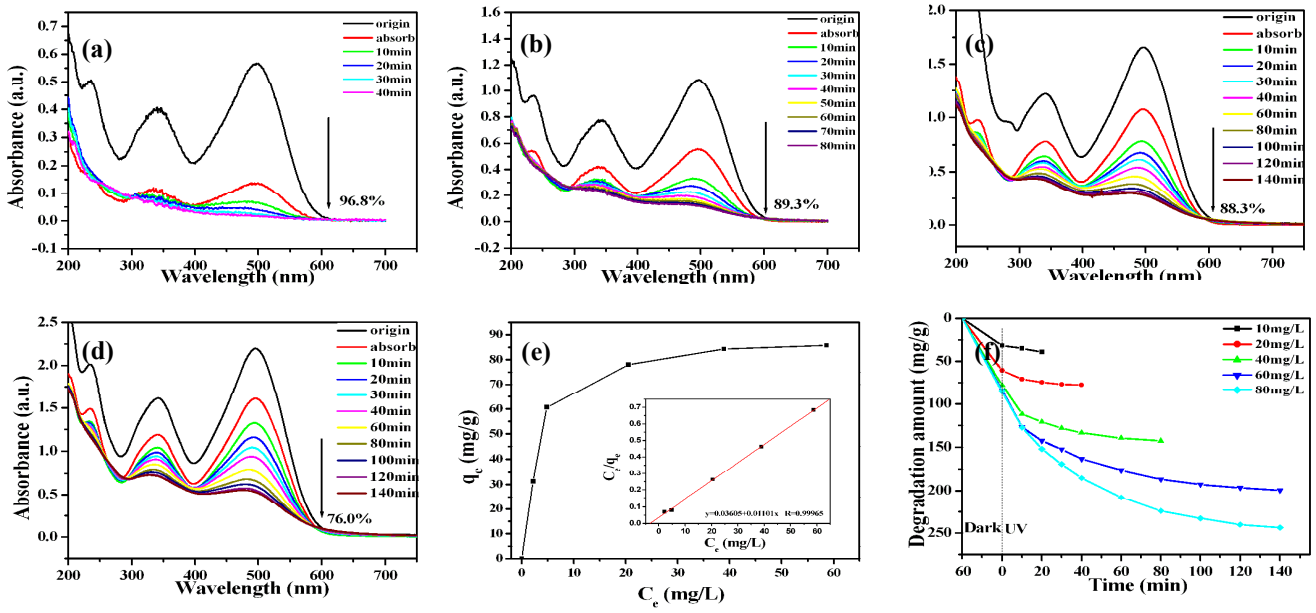

Fig. 8 Adsorption spectra of Congo red solution under UV light in the presence of ZnO/SnO_2-2 heterostructure nanofiber, (a) 20mg/L, (b) 40mg/L, (c) 60mg/L, (d) 80mg/L; (e) Effect of the initial dye concentration on the degradation capacity of ZnO/SnO_2-2 nanofiber, (f) Variation of the degradation capability of the ZnO/SnO_2-2 (dye/catalyst, mg/g) to degradation time.

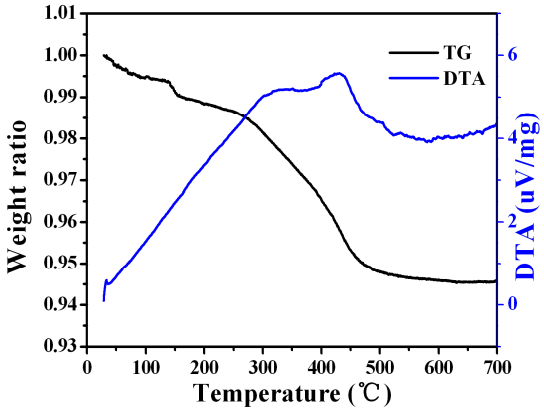

Fig. 9 Thermal gravimetry-differential thermal analysis (TG-DTA) curves of the ZnO/SnO_2-2 nanofibers after degradation of 20mg/L CR.

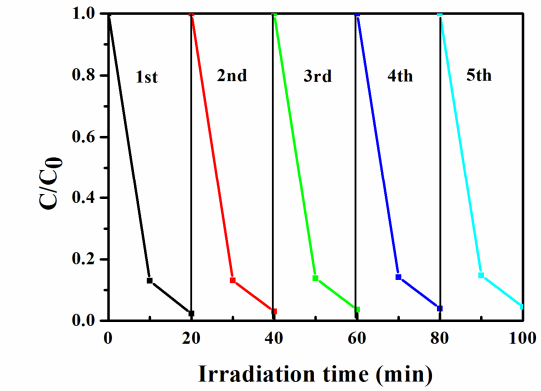

Fig. 10 Cycling tests of photocatalytic activity of the ZnO/SnO_2-2 heterostructure for Congo Red degradation

Sample	BET surface area (m^2 g^{-1})	Pore volume (cm^3g^{-1})	Pore diameter (nm)
ZnO/SnO2-1	30.175	0.101	3.3, 7.4
ZnO/SnO2-2	39.344	0.166	3.3, 5.4, 8.2
ZnO/SnO2-3	11.063	0.034	3.3, 5.4

Table1. Textural properties of the as-fabricated materials.